

FLOW IN A VORTEX CHAMBER

C.W. Hirt and R.P. Harper  
Flow Science, Inc.  
5/21/88

INTRODUCTION

There are many practical devices that employ fluid flowing with strong vortical components - for instance, cyclone separators, Hilsh tubes, mixers and toilets. In this note we investigate by numerical simulation the flow in a simple vortex chamber. The chamber consists of a segment of a right circular cylinder with a tangential inlet section and a circular outlet hole in the bottom. The outlet is offset with respect to the center of the cylindrical chamber. The inlet is also circular and has a diameter equal to the thickness of the chamber. Figure 1 shows a schematic of the geometry. The diameter of the chamber is 1.5 in and its thickness is 0.5 in. The circular inlet and outlet each have a diameter of 0.5 in.

For our simulation we assume water enters the inlet with a uniform velocity of 19.608 in/s, giving a flow rate of 6 gpm. The outlet pressure is assumed to remain at 0.0 psig corresponding to atmospheric pressure.

The purpose of this computation is to demonstrate how the Flow Science FLOW-3D computer program could be used to investigate many details associated with a variety of vortex flow instruments. In this particular case interest is in the basic flow and pressure distributions established in the vortex chamber under steady flow conditions. We shall, in fact, present two different computations. One computation has been carried out under the assumption of potential flow, while the other has been performed using a nearly inviscid version of the Navier-Stokes equations. As we shall see, the potential flow model is not appropriate for it misses the essential nature of the vorticity-dominated flow.

COMPUTATIONAL MODEL

FLOW-3D uses finite-difference approximations (or finite-volume approximations to be more precise) of the mass, momentum and energy equations for viscous fluids. The approximations are

made with respect to a grid of rectangular cells of variable size. To represent irregular obstacles and curved bounding walls a porosity technique called FAVOR is used in which the fractional face areas and fractional volumes of each grid cell open to flow are stored and used in the numerical approximations. Figure 2 contains cross section plots of the grid selected for the computations. A representation of the flow region carved out of the grid by the FAVOR scheme is given in the plots of Fig. 3. In the plot cutting through the inlet (left plot) it should be noted that there is an extra layer of grid cells along one side. This layer is used to define the circular outlet (right plot). In the middle plot of Fig. 3, which is a horizontal cut through the chamber about one half radius below the center of the inlet, we note that the plotter does not connect the vectors along the lower edge of the inlet channel. This defect is associated with the three-dimensional nature of the geometry and the fact that the plotter only has limited information available to reconstruct the geometry (i.e., the fractional areas and volumes of the grid cells). In the actual calculations the boundary is continuous.

Units employed in all calculations are inches and seconds with density in units of 12 slugs so that pressures are in psi. Water is assumed to be the working fluid, and we have treated it as an incompressible material because of the low flow speed.

A complete input file for this problem is given in Fig. 4. This FORTRAN "Namelist" file contains all the grid and obstacle definition data, the physical and computational parameters, and a selection of graphic output requests.

Results from two computations are described in the next sections. Both computations used the same input data with the exception of a couple of parameters that specified use of the potential flow option.

## IRROTATIONAL FLOW RESULTS

Because this is a steady flow problem, potential flow results should be established in one calculational step; but FLOW-3D is primarily a transient flow code so that it takes a couple of steps to fully establish consistent pressures and velocities. In particular, the pressures computed in the first step are those needed to accelerate the flow from zero to its steady state, then a second time step is needed to reset the pressures to their steady state values. For good measure we carried the computations through 10 time steps to be sure that steady flow conditions had been reached.

Computational results are displayed in Figs. 5-7. Referring to Fig. 5 we see that the flow simply enters the inlet and flows directly to the outlet. Much of the chamber has almost no flow at all, which is intuitively not realistic. The reason for this is that the potential flow assumption does not allow the incoming flow to "jet" into the chamber, which is a process that produces vorticity at the sharp boundary edge where the inlet tube intersects the circular wall of the chamber. In potential flow the fluid turns sharply around this corner and then flows directly to the outlet.

The computed pressures, shown in Fig. 6, reflect the basic flow pattern seen in Fig. 5. In particular, one should note the high pressure gradient located at the intersection of the inlet and chamber walls, which is responsible for the sharp turn in flow at that location.

#### ROTATIONAL FLOW RESULTS

In the second calculation the potential flow option was turned off and the full FLOW-3D solution algorithm was employed for the fluid conservation equations. Because the Reynolds number for this problem is about 6300, based on the inlet flow speed and inlet diameter, viscous effects must be rather small. For example, viscous boundary layers on the walls of the chamber are expected to be much thinner than the size of the grid cells. Since we cannot resolve such details, we have chosen to neglect all viscous effects by using a zero value of viscosity.

Even though we are neglecting viscosity, this does not mean that vorticity cannot be generated. As observed in the potential flow case, vorticity can be generated at the trailing edge of the inlet and then transported by advection into the interior of the vortex chamber.

It is important to recognize that there will be some smoothing of the computed velocities because of the discreteness of the computational grid (i.e., within each grid cell there must be some averaging or smoothing of the velocity changes computed for the cell). While this numerical smoothing is sometimes referred to as numerical viscosity, it is not a viscosity and does not have the same tensor properties exhibited by real viscous stresses. Nevertheless, we must be careful in the interpretation of the computed results. For instance, numerical smoothing will largely prohibit any breakdown into fine scale turbulence even though that might happen in a physical experiment.

To achieve steady state results it is necessary to process the solution through many time-step cycles in order to get vorticity advected throughout the entire flow field. One way to speed up the attainment of steady conditions is to relax the accuracy of the transient portion of the calculation. In FLOW-3D this is done by limiting the pressure iteration algorithm, which is used to satisfy the incompressibility condition, to only one iteration per cycle. We do this by using a large convergence criteria ( $\text{EPSI}=1.0\text{E}+6$ ) and no overrelaxation ( $\text{OMEGA}=1.0$ ). Although the computed flow transients may not be correct, because the flow doesn't strictly remain incompressible, this reduces the computational overhead in a given cycle so that many cycles can be processed. The goal is to accumulate lots of advection cycles with a minimum amount of computer time.

### Overview of Computed Results

Computed results at steady conditions are contained in Figs. 8-10. A brief comparison between Figs. 8-10 and Figs. 5-7 shows that there is a qualitative difference in these results compared with the potential flow case. A swirling flow is now present throughout the chamber. As expected, the inlet flow propagates more or less straight into the chamber striking the wall opposite the inlet. Deflection then causes this flow to spiral down to the outlet, Fig. 9. The core of the vortex flow is slightly tilted with its bottom (outlet) end closer to the inlet than its top end.

It may also be observed that the maximum velocity in the chamber is significantly larger than the inlet velocity. There are at least two reasons for this. First, a flow acceleration occurs, which is largest near the bottom of the chamber, because of convergence of the swirling flow with the inlet jet. Second, the displacement of the outlet with respect to the center of the chamber requires the swirling flow to move to progressively smaller radii before exiting the device, which results in an azimuthal acceleration to preserve angular momentum.

Pressure distributions for this case are shown in Fig. 10. We see little pressure variation around the side wall of the chamber opposite the inlet. The principal variation in pressure is radial and is a result of the swirl. A very small negative pressure (i.e., below atmospheric pressure) is observed at the core of the vortex. This is shown most clearly in Fig. 8. A comparison of Fig. 8 with Fig. 7 illustrates another difference with the potential flow case; the potential flow did not exhibit a pressure undershoot and the total pressure drop was only about a third of that computed with the full Navier-Stokes equations.

Figure 8 further indicates that in the right half of the chamber, away from the inlet and outlet, the pressure is nearly uniform between the top and bottom surfaces. This result is partly a consequence of the neglect of viscous shear stresses at the bounding walls, but more importantly it shows that details of the circular inlet geometry have been washed out by the time the incoming flow reaches the opposite wall of the chamber.

### Discussion of Computed Results

The average pressure at the inlet,  $P_0$ , is approximately 0.031 psig. Although the pressure does not vary much across the inlet cross section it is slightly lower near the bottom of the chamber. The dynamic head,  $\rho v^2/2$ , of the specified inlet flow is 0.018 psi, which we shall denote by PH.

At the outlet we specified a uniform pressure, but reference to Fig. 8 indicates that there are relatively large pressure gradients immediately above the outlet plane. This suggests that it might have been better to define a longer outlet pipe with a length at least equal to the diameter of the outlet to minimize the influence of this boundary condition on upstream flow conditions. In any case, the net pressure drop between the inlet and outlet is about 0.031 psi, or  $1.72*PH$ . A complete stoppage of the inlet flow and its redirection into another uniform flow moving in a perpendicular direction would require an average pressure increase at the turning point of  $2.0*PH$ , so the somewhat smaller computed value is realistic.

It should also be noted that the outlet flow has a pronounced swirl component. In this connection the slight negative pressure at the core of the vortex might become low enough at higher flow speeds to cause cavitation.

The maximum pressure in the chamber is near the midplane of the chamber and at a wall position of about 4 o'clock (where the inlet is at the 10-11 o'clock position). The maximum pressure is approximately 0.07 psia, or  $P_0 + 2.16*PH$ . An increase of  $2*PH$  above the inlet pressure is reasonable based on the above observation about a turning flow. The fact that the computed factor is slightly larger than 2.0 is probably a reflection of the local increase in flow speed caused by the convergence of the swirling flow with the inlet jet.

### Other Considerations

In viewing these results it must be remembered that we have only performed one computation and that this computation was made with certain assumptions. For example, we have already mentioned that it might be a good idea to lengthen the outlet line to

reduce any influence of a uniform pressure assumption at the outlet. If viscous effects were to be added to the simulations, then we might expect to see some Eckman-type secondary flows generated in the corners of the vortex chamber. Certainly, at higher flow speeds we must also expect turbulence to be an important feature of the flow. Furthermore, it is likely that the inlet flow will not be uniform as we assumed, but will have a laminar or turbulent profile that is characteristic of steady flow conditions in the inlet line.

All of these model variations could be investigated with additional FLOW-3D calculations. Most importantly, it would be desirable to have some well instrumented laboratory tests to use as benchmark validation tests for the computations. Comparison with physical tests is the best way to learn how to interpret the computational results and to gain confidence in their use.

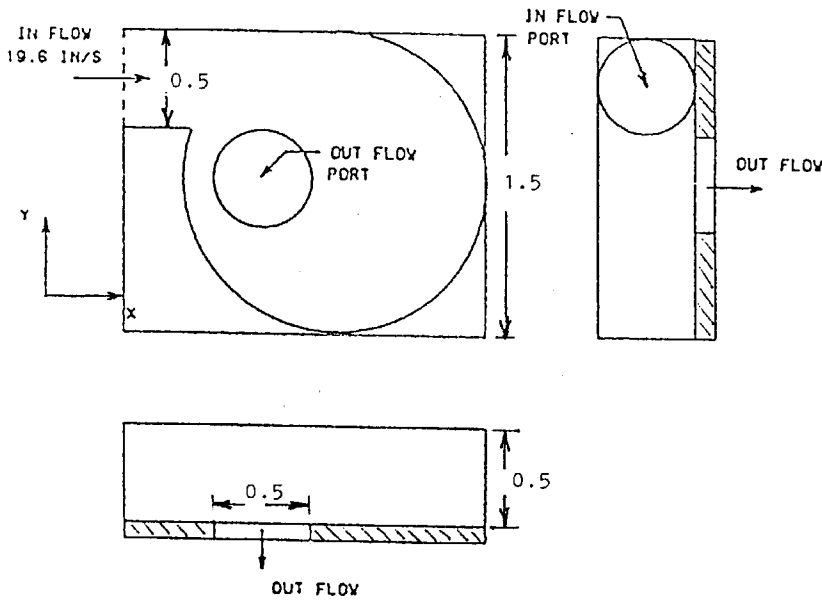


Fig. 1. Schematic showing problem geometry.

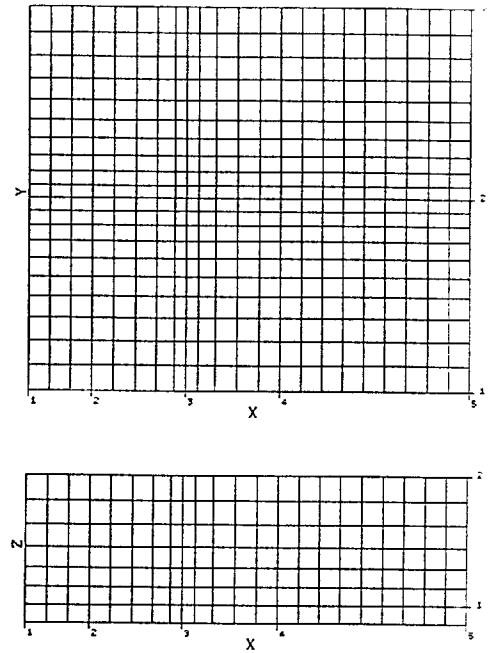
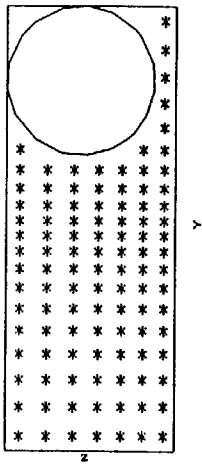
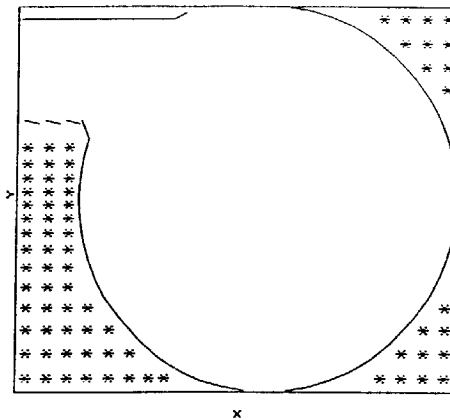


Fig. 2. Finite-difference grid used for calculations.

OBSTACLE PLOT (Y-Z PLANE AT I= 2)



OBSTACLE PLOT (X-Y PLANE AT I= 4)



OBSTACLE PLOT (X-Y PLANE AT K= 2)

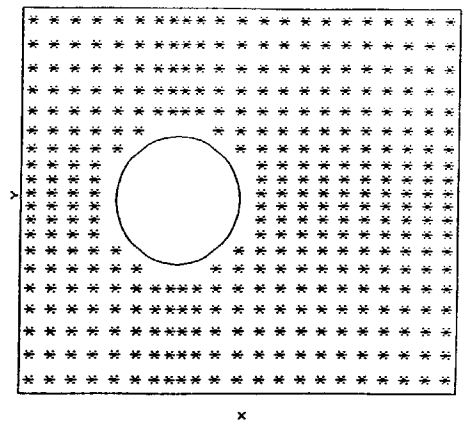


Fig. 3. Preprocessor plots used to check geometric setup. Inlet (left), chamber, (center) and outlet (right).

VORTEX FLOW

\$XPUT

WL=6,  
 WBK=2,  
 UBCT(1,1)=19.608,  
 CON=0.45,  
 PRTDT=1.0,  
 EPSI=1.0E+6,

WR=2,  
 WT=2,  
 PBCT(1,5)=0.0,  
 AVRCK=-2.1,  
 PLTDT=0.05,  
 TWFIN=0.2,

WF=2,  
 WB=5,  
 RHOF=0.936E-4,  
 DELT=0.001,  
 OMEGA=1.0,

\$END

\$MESH

NXCELT=22,  
 PX(1)=-1.0,  
 PX(4)=0.0,  
 NYCELT=20,  
 PY(2)=0.0,  
 NZCELT=6,

PX(2)=-0.75,  
 PX(5)=0.75,  
 PY(1)=-0.75,  
 PY(3)=0.75,  
 PZ(2)=0.5,

PX(3)=-0.375,  
 SIZEX(3)=0.05,  
 SIZEY(2)=0.05,  
 SIZEZ(1)=0.07,

\$END

\$OBS

NOBS=2,  
 IOFO(1,1)=1,  
 CC(1)=0.5625,  
 IOFO(2,1)=2,  
 IOH(2)=0,  
 CZ(2)=-0.5,  
 IOFO(1,2)=3,  
 IOFO(2,2)=4,  
 CY2(4)=1.0,

CX2(1)=-1.0,  
 XH(2)=0.0,  
 CZ2(2)=1.0,  
 CC(2)=0.25,  
 CZ(3)=1.0,  
 IOH(4)=0,  
 CX(4)=0.75,

CY2(1)=-1.0,  
 CY2(2)=1.0,  
 CY(2)=-1.0,  
 CC(3)=0.0001,  
 CX2(4)=1.0,  
 CC(4)=0.0781,

\$END

\$FL

\$END

\$BF

\$END

\$TEMP

\$END

\$GRAFIC

NCPLTS=4,  
 KC1(2)=5,  
 JC1(4)=11,  
 NVPLTS=4,  
 KV1(2)=5,  
 JV1(4)=11,  
 IOBSL=2,

KC1(1)=3,  
 KC2(2)=5,  
 JC2(4)=11,  
 KV1(1)=3,  
 KV2(2)=5,  
 JV2(4)=11,

KC2(1)=3,  
 KC1(3)=8,  
 KV2(1)=3,  
 KV1(3)=8,

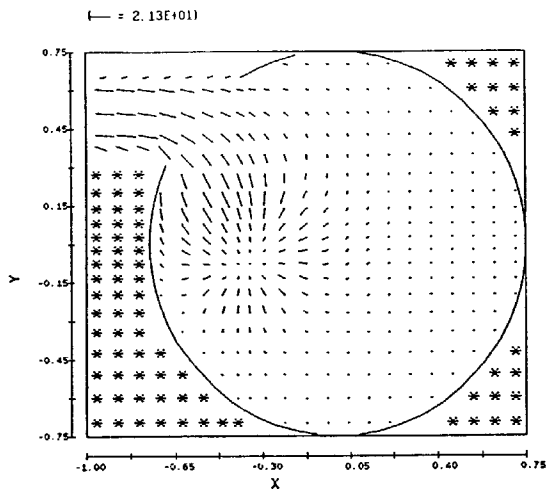
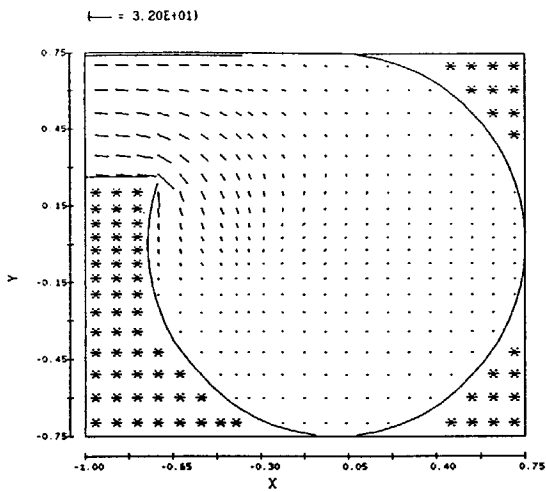
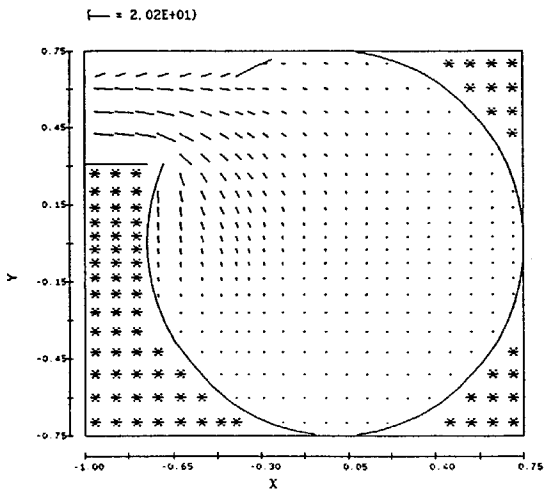
\$END

\$PARTS

\$END

Fig. 4. Complete input file used for rotational case.

VELOCITY VECTORS



PRESSURE CONTOURS

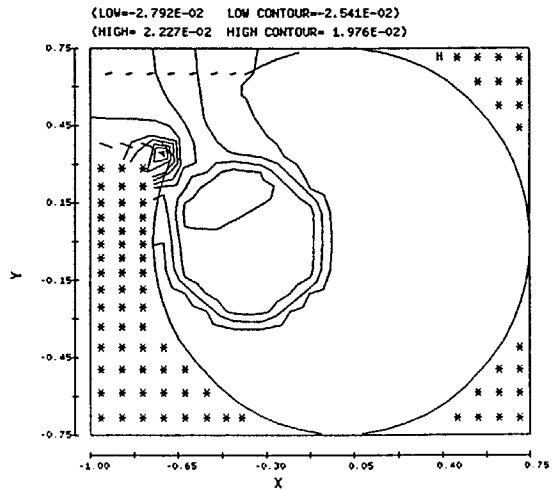
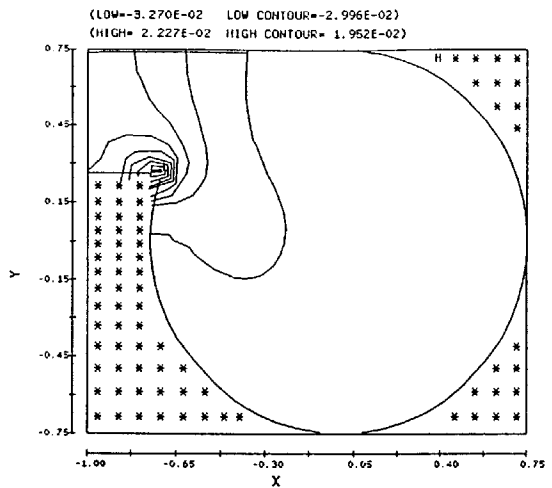
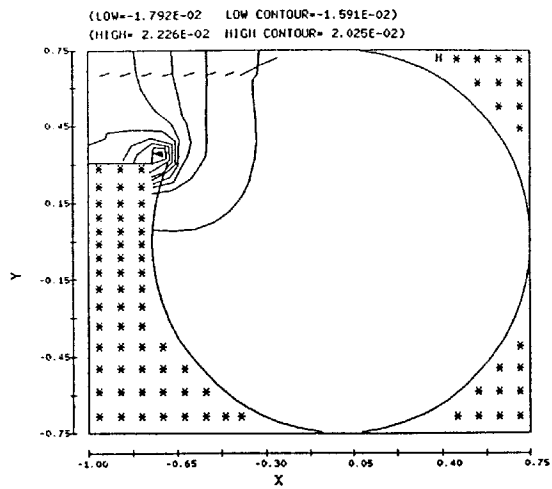
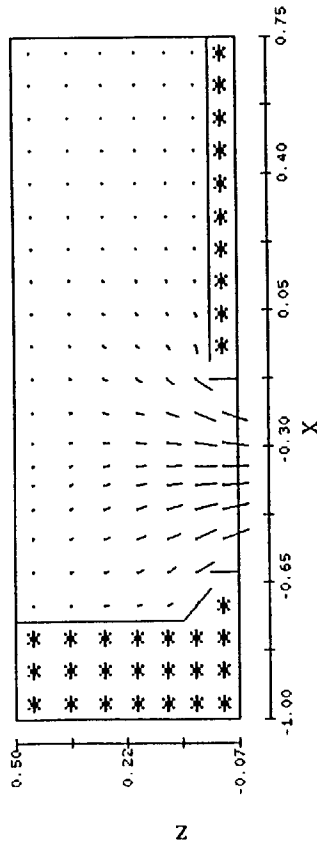


Fig. 5. Velocity plots for potential flow: top of chamber (top), middle of chamber (middle) and bottom of chamber (bottom).

Fig. 6. Potential flow pressure contours corresponding to Fig. 5 velocities.

VELOCITY VECTORS

(— = 2.12E+01)



PRESSURE CONTOURS

(LOW= 0.000E+00 LOW CONTOUR= 1.104E-03)  
(HIGH= 2.207E-02 HIGH CONTOUR= 2.097E-02)

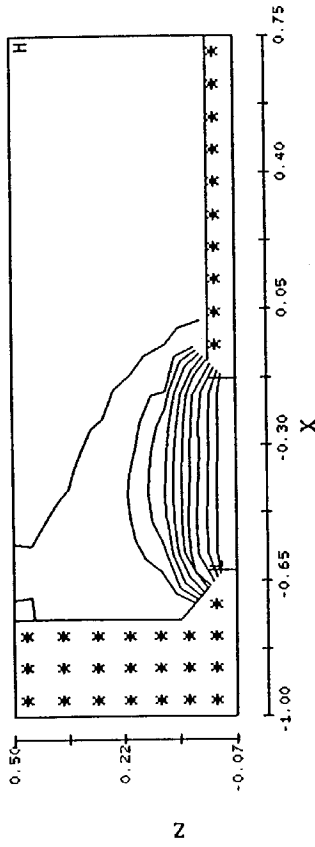
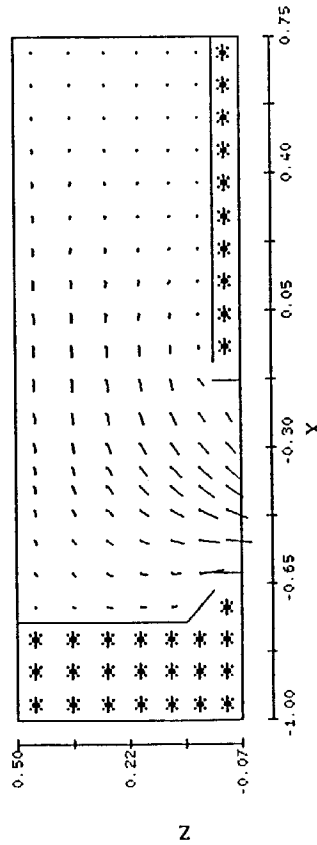


Fig. 7. Velocities (left) and pressures (right) for potential flow in vertical slice through chamber. Slice runs from 9 o'clock to 3 o'clock where inlet is at 10-11 o'clock.

VELOCITY VECTORS

(— = 2.46E+01)



PRESSURE CONTOURS

(LOW=-2.056E-03 LOW CONTOUR= 1.430E-03)  
(HIGH= 6.766E-02 HIGH CONTOUR= 6.418E-02)

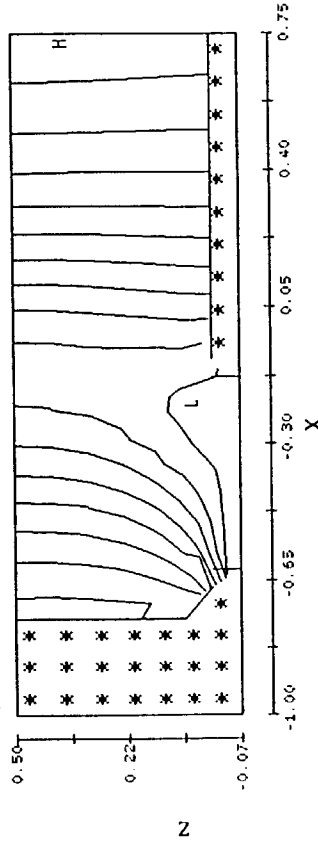


Fig. 8. Velocities (left) and pressures (right) for rotational flow in vertical slice through chamber. Slice runs from 9 o'clock to 3 o'clock where inlet is at 10-11 o'clock.

